

Quantifying Global-Warming Response of the Orographic Precipitation in a Typhoon Environment with Large-Eddy Simulations

Jianan Chen^a and Xiaoming Shi^a

^a *Division of Environment and Sustainability, Hong Kong University of Science and Technology,*

Hong Kong, China

Corresponding author: Jianan Chen, jianan.chen@connect.ust.hk

Preprint statement

This manuscript is non-peer reviewed preprint and has been submitted to Journal of Climate for peer review.

1 **Quantifying Global-Warming Response of the Orographic Precipitation in**
2 **a Typhoon Environment with Large-Eddy Simulations**

3

4

Jianan Chen^a and Xiaoming Shi^a

5

^a *Division of Environment and Sustainability, Hong Kong University of Science and Technology,*

6

Hong Kong, China

7

Corresponding author: Jianan Chen, jianan.chen@connect.ust.hk

8

ABSTRACT

9 The intense and moist winds in a tropical cyclone (TC) environment can produce strong
10 mountain waves and substantially enhanced precipitation over complex terrain, yet few
11 studies investigated how the orographic precipitation in a TC environment might respond to
12 global warming. Here, we use large-eddy simulation to estimate the global warming-induced
13 change in the precipitation over and near an idealized mountain with pseudo-global warming
14 experiments. Two regions in the simulations exhibit locally enhanced precipitation, one over
15 the mountain and the other in the downstream region 25 to 45 km away from the mountain.
16 The enhanced precipitation in both regions is related to the seeder-feeder mechanism, though
17 the enhancement in the downstream regions differs from the conventional definition and is
18 referred as pseudo-seeder-feeder mechanism (PSF). In the PSF mechanism, mountain waves
19 generate an intense cloud formation center in the mid-troposphere above the lee slope, and
20 the resulting precipitation particles drift downstream, intensifying downstream convection
21 when they fall into proper locations and heights. Under warming, the precipitation maximum
22 over the mountain exhibits minimal change, while the precipitation maximum in the
23 downstream region exhibiting sensitivity of around $18\% \text{ K}^{-1}$ intensifies and shifts towards
24 the mountain. The small sensitivity of the first precipitation peak is due to the canceling
25 effects of thermodynamic and dynamic changes. The large sensitivity in the downstream
26 region is mainly due to the strengthening of the wave-induced mid-troposphere cloud
27 formation center which supplies more hydrometeors to the downstream region and enhances
28 precipitation efficiency through the enhanced PSF mechanism.

29

30

SIGNIFICANCE STATEMENT

31 The combination of typhoon environment and orography can produce intense precipitation
32 and thereby severe flooding risks. Here, we investigate the global-warming response of
33 orographic precipitation in a typhoon environment with idealized, high-resolution
34 simulations. The experiments suggest that under warming, a precipitation maximum may
35 emerge in the downstream region of a mountain, or strengthen and shift upwind if it already
36 exists in the current climate. This surprising amplification of downstream region precipitation
37 is related to the enhancement of the mid-tropospheric cloud generation caused by mountain
38 waves and has critical implications to flooding risk management in mountainous regions.

39 **1. Introduction**

40 The mountains and their foothills are dwelling places for around 26% of the global
41 population (Beniston 2005). An essential source of water supply in the mountainous region is
42 orographic precipitation (Schär and Frei 2005). Yet, heavy orographic precipitation can also
43 induce flash floods and subsequently bring social and economic damages to human society
44 (Houze 2012). It's therefore of critical importance to assess how the orographic precipitation
45 will change in response to the warming climate.

46 Global warming can affect orographic precipitation through modification of thermodynamic,
47 dynamic, and cloud microphysics factors. Under global warming, with roughly unchanged
48 relative humidity, the water vapor in the atmosphere will increase by $\sim 7\% \text{ K}^{-1}$ of surface
49 warming based on the Clausius–Clapeyron (CC) equation (O’Gorman 2015). The increased
50 moisture in a warmed climate is expected to increase precipitation over mountains. For
51 example, Jing et al. (2019) show that in their pseudo-global warming simulations, the
52 projected increase of wintertime precipitation in the interior western United States mountains
53 under global warming is mainly induced by increased moisture with other factors playing
54 secondary roles. Nonetheless, the increased temperature and moisture can alter the gravity
55 wave dynamics which can further affect the precipitation. Shi and Durran (2015) conducted
56 an idealized study to investigate the orographic precipitation over idealized north-south
57 oriented midlatitude mountain barriers and found the extreme precipitation over the eastern
58 slope increases at a rate higher than that over the western slope. The relatively strong
59 response over the eastern slope is explained by the vertical velocity change which is governed
60 by gravity wave dynamics. The change in atmospheric stability and cross-mountain wind
61 speed is critical because they determine whether the incoming airstream is blocked by the
62 mountain of interest (Eidhammer et al. 2018; Kirshbaum et al. 2018). In the blocked case, the
63 incoming airstream tends to deflect around the mountain instead of passing over it
64 (Kirshbaum et al., 2018); without substantial forced lifting, heavy precipitation is less likely
65 to occur. Large-scale circulation shifts under warming can affect where the precipitation
66 forms through the moisture transport (Shi and Durran, 2014). The warming response of
67 microphysical processes occurring in clouds has been investigated in several studies
68 (Kirshbaum et al. 2018). Kirshbaum and Smith (2008) found that precipitation efficiency
69 (PE) will decrease in response to warming because the mixed-phase rain processes are partly
70 replaced by the less efficient warm rain process. Pavelsky et al. (2012) show that the lifted

71 freezing level in a warmed climate may cause an upwind shift of orographic distribution.
72 With a higher freezing level, falling hydrometeors from upper levels will shift from solid
73 phase to liquid phase earlier. Considering the faster falling speed of liquid hydrometeors, the
74 hydrometeors will fall in a shorter distance and therefore cause an upwind shift in the
75 precipitation distribution (Pavelsky et al. 2012).

76 Some of the most intense precipitation events happen when tropical cyclones (TCs) pass over
77 complex terrain (Houze 2012; Smith et al. 2009). A TC can produce heavy rainfall directly in
78 its spiral rainband and eyewall, or indirectly through the interaction between its circulation
79 with mountain ranges (Wang et al. 2009). When a steep mountain range intersects with TC
80 circulation, the environmental conditions featuring strong surface wind, moist air, and low
81 static stability are consistent with empirical conditions favoring the occurrence of intense
82 orographic precipitation (Lin et al. 1998). However, previous research has not investigated
83 how the orographic precipitation induced by the interaction between mountain range and TC
84 outer region circulation will change in response to warming. This might be due to two
85 reasons. Firstly, it is computationally infeasible to simulate a TC spanning thousands of
86 kilometers horizontally with large-eddy simulation (LES) resolution that can explicitly
87 resolve the fine-scale process (Bryan et al. 2017). The use of convection parameterization is
88 often accused of being the reason for inconsistent prediction of extreme precipitation
89 sensitivities to warming in climate models (Muller, 2013; O’Gorman, 2015). To avoid the
90 uncertainties brought by the convection parameterization schemes, convection-permitting
91 models with horizontal grid spacings on the order of one kilometer have been employed to
92 investigate the warming response of convective systems (Guichard and Couvreur 2017;
93 Kirshbaum and Smith 2008). However, the kilometer-scale resolution is in the gray zone of
94 convection and terrain (for smaller mountains) and how to resolve gray zone issues is an
95 ongoing topic (Chow et al. 2019). LES can help avoid those uncertain issues, but it is
96 computationally demanding to conduct three-dimensional typhoon simulations at the
97 resolution of ~100 m. Secondly, a direct comparison is hard to achieve because TC outer
98 region rainband is highly asymmetric, therefore, even in pseudo-global warming experiments
99 (Schär et al. 1996; Trapp et al. 2021), it is difficult to ensure the same timing for a preexisting
100 convective system or moisture plume to impinge on a mountain. As a result, it is hard to tell
101 whether orographic precipitation differences in the experiments are due to warming or timing
102 (i.e., preexisting convective system may impinge onto the mountain at different stages of the
103 life cycle of the system).

104 To overcome those difficulties, we adopted the LES method developed by Bryan et al.,
105 (2017) (hereafter B17) to simulate the TC environment. Instead of simulating the entire TC,
106 this LES method only simulates a small ‘patch’ of a typhoon. The large-scale conditions that
107 dominate the small ‘patch’ are specified using prescribed input parameters. Therefore, the
108 large-scale conditions can be controlled to ensure direct comparisons. The warming
109 experiments of the LES simulations are conducted with the pseudo-global warming method.
110 (Rasmussen et al. 2011). We will focus on the intensity and distribution changes in
111 orographic precipitation due to warming and investigate the underlying mechanisms.

112 **2. Experiment setup**

113 *a. Typhoon Case*

114 The LES simulations have an idealized environment based on a real typhoon event. Typhoon
115 Vicente (2012) is one of the strongest typhoons affecting Hong Kong (HK) in recent decades
116 and it caused more than 200 mm of precipitation over the two-day period during its passage
117 over HK (Hong Kong Observatory 2012). According to observation data, the strongest
118 precipitation in HK occurred 12 hours after Vicente’s landfall, when Vicente was more than
119 300 km away from HK. During the period from 05:00 UTC and 07:00 UTC on 24th July
120 2012, intense precipitation happened in Hong Kong.

121 During the two-hour intense precipitation period, Hong Kong happened to be located nearly
122 due east of the cyclone center and indicated by the black square box in Supplementary Fig.
123 S1. Therefore, for simplicity, no rotation of the wind profile was applied when setting the
124 LES domain, and the tangential wind for the LES domain is assumed from due south. The
125 square box in Supplementary Fig. S1 is centered at the Lantau Island of Hong Kong with a
126 side length of 100 km. The Radius from the low-pressure center of the typhoon to the square
127 center is 338.84 km. The Weather Research and Forecast (WRF) was used to simulate
128 Typhoon Vicente in a previous study (Shi and Wang 2022) with horizontal resolution down
129 to 1.6 km. We use the WRF simulation data to determine the input parameter profiles for base
130 state and initial conditions of our LES simulation, by averaging relevant variables in the
131 small square region in Supplementary Fig. S1 and over the 2-hour period with the most
132 intense precipitation.

133 *b. LES Simulation Setup*

134 For our LES simulations, we use the TC environment parameterization method developed by
135 Bryan et al. (2017) for the non-hydrostatic numerical model Cloud Model 1 (CM1, version
136 20.3) (Bryan and Fritsch 2002), which is an advanced tool for idealized LES and convection-
137 permitting simulations. The LES domain consists of $N_x = 256$ grid points in the x direction
138 with $\Delta x = 200$ m and a total length of $L_x = 51.2$ km. In the y direction, there are $N_y = 512$ grid
139 points, with $\Delta y = 200$ m and a total length of $L_y = 102.4$ km. In the vertical direction, the
140 model has $N_z = 128$ levels, with the grid spacing Δz stretching from 150 m near the surface to
141 500 m at the model top ($L_z = 31.2$ km). Periodic boundary conditions are applied at both
142 horizontal directions. The Rayleigh damping is applied at heights above 22 km to avoid the
143 excessive spurious reflection of gravity waves. The research is conducted mainly using the
144 Thompson scheme (Thompson et al. 2008) as the microphysics scheme. For testing
145 robustness of our conclusions, we also conducted some simulations with the Morrison
146 microphysics scheme (Morrison et al. 2009) and documented the results in Section 6. For
147 subgrid-scale turbulence parameterization, we used the TKE scheme (Deardorff 1980), and
148 radiation is computed using the rapid radiative transfer model for general circulation models
149 (RRTMG) (Iacono et al. 2008).

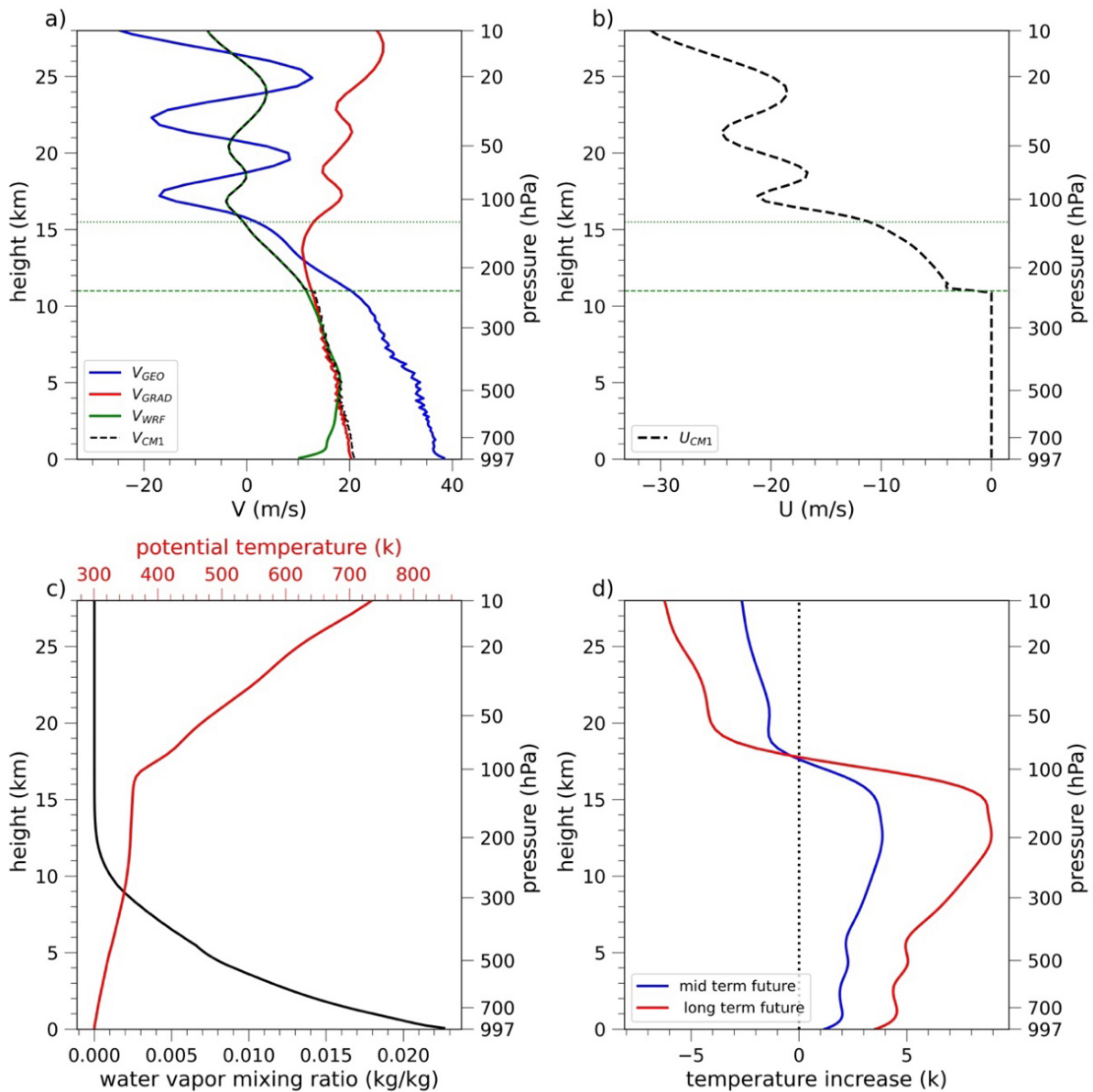
150 The B17 method was originally designed for simulating the wind profiles in the boundary
151 layer of the outer region in TC. In this study, to investigate the interaction between
152 convections and the mountain, the method is adapted, and the LES domain extends to 31.2
153 km in height. The TC boundary wind profile simulation model in B17 is based on the
154 assumption that the small LES domain (embedded within the TC environment) is subject to
155 centrifugal and advection accelerations that apply at scales large than the domain. The
156 fundamental idea of B17 is to account for these large-scale conditions by specifying the
157 vertical profile of gradient wind speed V , the radial gradient of gradient wind speed $\frac{\partial V}{\partial R}$, and a
158 distance away from the tropical cyclone center R . Other than these parameters, to initiate the
159 simulation, the vertical profile of potential temperature (θ), water vapor mixing ratio (q_v) are
160 needed and shown in Fig. 1. B17 suggests that the $\frac{\partial V}{\partial R}$ can be related to $\frac{V}{R}$ through a decay rate
161 n , $\frac{\partial V}{\partial R} = -n \frac{V}{R}$. The decay rate n for all types of tropical cyclones ranges from 0.04 to 0.64
162 (Mallen et al. 2005). We've found the precipitation intensity and distribution are insensitive
163 to the selection of decay rate in this range. In view of this, a decay rate of 0.6 is used. The
164 distance between the center of our research domain and the low-pressure center R is 338.84
165 km.

166 The large-scale pressure gradient in B17, originally designed for the atmospheric boundary
167 layer, is derived from the gradient wind balance relationship. However, the gradient wind
168 balance no longer holds at higher levels where there is no well-defined circular low-pressure
169 center. Figure 1a shows the profile of meridional velocity V_{WRF} derived from the temporal
170 and spatial mean of V from WRF output data, geostrophic wind V_{GEO} calculated based on the
171 geostrophic balance, and V_{GRAD} calculated from the gradient wind balance. Below $z_1=11$ km,
172 V_{WRF} is consistent with V_{GRAD} except at the levels near surface, suggesting that in the lower
173 and middle troposphere, the large-scale wind field is well approximated by the gradient wind
174 balance in which the pressure gradient force is balanced by centrifugal force and Coriolis
175 force. The inconsistency between V_{WRF} and V_{GRAD} at the lowest levels is due to the
176 unaccounted surface friction and boundary-layer flux. Above $z_2=15.5$ km indicated by the
177 green dotted horizontal line, the V_{WRF} oscillates around zero and shows good agreement with
178 V_{GEO} , suggesting the wind field follows the geostrophic balance in which the large-scale
179 pressure gradient is balanced only by the Coriolis force. At heights between z_1 and z_2 , the
180 wind field transitions from the gradient wind balance to the geostrophic wind balance, in
181 which the centrifugal force gradually disappears.

182 In our setup of the large-scale pressure gradient in LES, for simplicity, we apply a linear
183 decay coefficient α on the centrifugal force term and assume α decreases from unity at height
184 z_1 to zero at height z_2 to represent the disappearance of centrifugal force. At levels above z_2 ,
185 with no presence of centrifugal forces, we specify the large-scale pressure gradient force
186 based on the geostrophic wind balance by setting α as 0. In the LES method of B17,
187 mesoscale tendency terms are associated with the mesoscale flows in the tropical cyclone.
188 Similarly, we apply the same decay coefficient α on the mesoscale tendency terms.

189 The original B17 method focuses on simulations of the wind profiles in the dry atmosphere.
190 Moisture effects are neglected. Similar to Chen et al. (2021), nudging terms are applied to the
191 tendency of temperature, specific humidity, and large-scale wind for the purpose of
192 accounting for the effects of the large-scale circulation of typhoon environment. Details are
193 be found in equations (1b) and (1c) from Chen et al. (2021). This nudging approach ensures
194 that the large wind profiles, temperature, and moisture remain anchored throughout the
195 simulations. The nudging relaxation timescale we used is 2 hours.

196



197

198 Fig. 1. (a) and (b) show the vertical profiles of horizontal wind (V and U). The mean V
 199 profile derived directly from the WRF simulation are denoted by the solid green line. The
 200 mean V profiles calculated based on the geostrophic wind balance are shown as the solid blue
 201 lines and labeled as V_{GEO} . The V profile calculated based on the gradient wind balance is
 202 shown as the solid red line and labeled as V_{GRAD} . The dashed black lines show the input
 203 V, U profiles used in our simulation and are labeled as V_{CMI} and U_{CMI} , respectively. (c)
 204 Potential temperature derived directly from the WRF simulation and water vapor mixing ratio
 205 (q_v). The q_v is derived assuming the atmosphere is saturated. (d) The CMIP6 predicted
 206 temperature increase of mid-term future climate (blue line) and long-term future (red line)
 207 relative to present climate.

208

209 The terrain profile and initial flow field are specified by several parameters. The idealized
 210 bell-shaped terrain is set up to loosely mimic the Hong Kong topography which is featured by

211 west-east-oriented mountains. The surface elevation Z_s of this bell-shaped mountain is
212 specified as

$$Z_s(y) = \begin{cases} \frac{h_0}{2} \left(1 + \cos \left(\pi \left(\frac{y - y_m}{a} \right) \right) \right) & \text{if } y_m - a < y < y_m + a \\ 0 & \text{else} \end{cases} \quad (1)$$

213 where the maximum height h_0 is 1 km, half-width a is 10 km, $y_m = 0$ is at the center of the
214 domain in the meridional direction. The surface area where $Z_s = 0$ is set as ocean surface. The
215 mountain is symmetric in the zonal x direction.

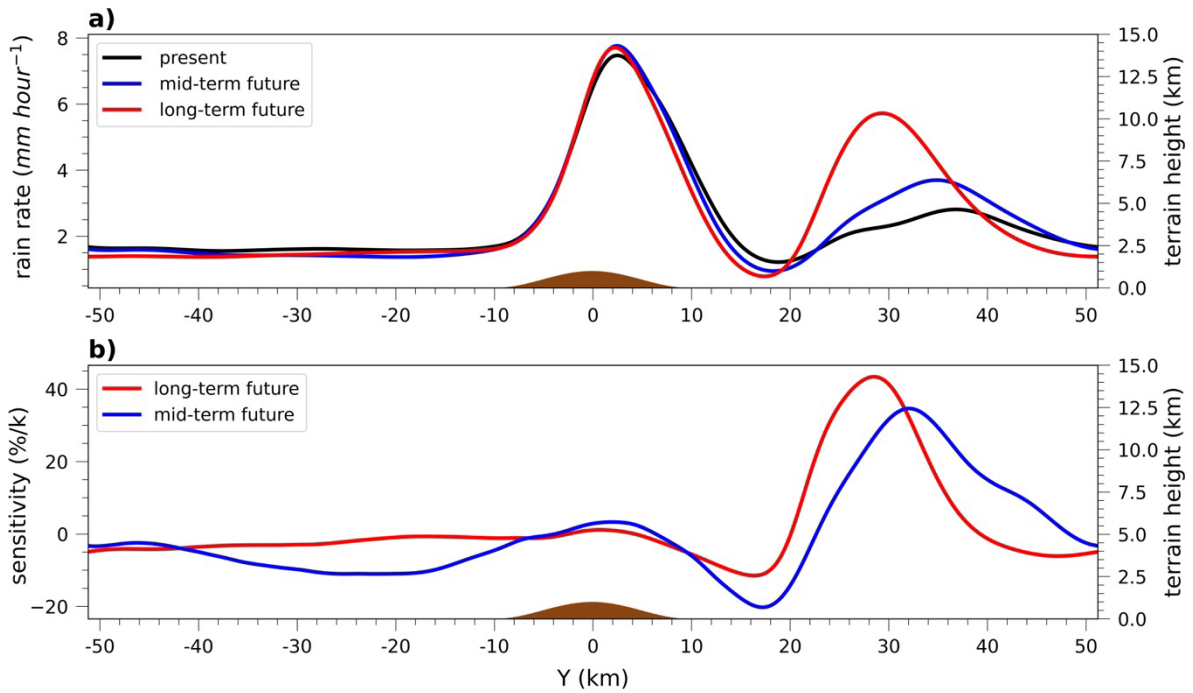
216

217 *c. Warming Experiments*

218 In the warming experiments, we've conducted pseudo-global warming by adding the
219 temperature change predicted by the SSP5-8.5 (Shared Socioeconomic Pathway) warming
220 scenario from the Coupled Model Intercomparison Project phase 6 simulations (CMIP6) onto
221 the control simulation temperature profile. The current climate state is defined as the average
222 for the period of 2015-2020, the mid-term future as the period of 2050-2060, and the long-
223 term future as the period of 2090-2100. The temperature is averaged over the larger domain
224 centered at Hong Kong, ranging from 110 to 120 degree in longitude and 15 to 25 degree in
225 latitude. The surface warming relative to the present climate is 1.18 and 3.53 K, respectively,
226 for the climate of the mid-term future and long-term future. Figure 1d shows temperature
227 change between present climate and future climates. The temperature anomaly profiles are
228 characterized by the strongest warming happening in the upper troposphere, and the cooling
229 happening in the stratosphere, consistent with previous studies (e.g., Ji et al., 2020). In the
230 troposphere, the upper levels exhibit stronger warming than the low levels, suggesting a more
231 stable atmosphere under warming. In terms of the input of vertical profile of q_v , we assume
232 the relative humidity profile remains constant over the warming. Therefore, we have 3 groups
233 of simulations: present, mid-term future, and long-term future climate. Each simulation was
234 integrated for 36 hours with an output interval of 10 min. The first 12 hours are discarded as
235 the spin-up period. In the analysis below, unless otherwise specified, the temporal average is
236 taken over the period from hour 12 to hour 36.

237 **3. Orographic Precipitation and Traveling Convective System**

238 *a. Precipitation Distributions*



239

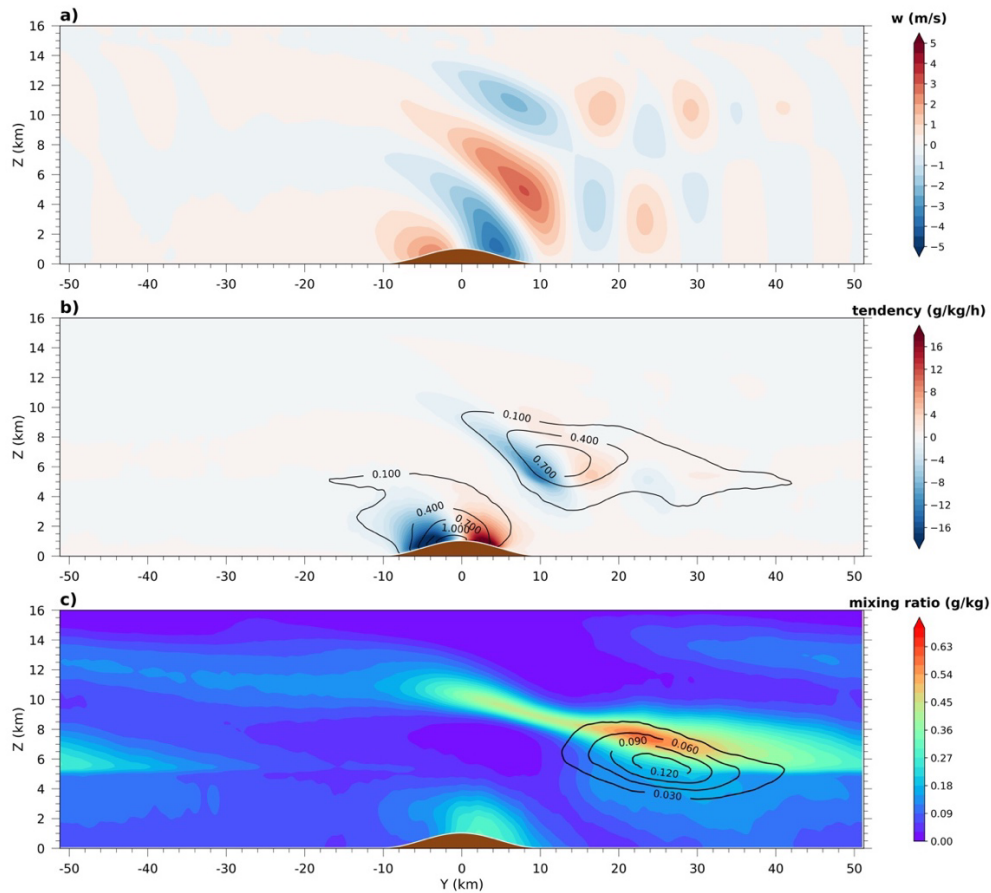
240 Fig. 2. (a) The zonal and temporal mean precipitation distribution in the simulations of
 241 present, mid-term future, and long-term future climate. (b) the corresponding precipitation
 242 sensitivity distribution of mid-term future and long-term future climate in (a). The
 243 sensitivities in (b) are defined relative to the present climate.

244

245 The zonal (x -direction) and temporal mean precipitation distributions are shown in Fig. 2. In
 246 the simulation of the present climate, two local precipitation maxima can be identified. The
 247 first precipitation maximum is located on the lee slope of the mountain and the second
 248 precipitation peak is in the downstream of the mountain at around 37 km. The simulations for
 249 mid-term future and long-term future climate exhibit qualitatively similar precipitation
 250 maxima patterns with peaks on the lee slope and in the downstream region.

251 The first precipitation peak on the mountain slope barely changes (shown in Fig. 2a) with
 252 warming. By contrast, the second downstream region precipitation peak shifts upwind
 253 towards the mountain and intensifies substantially with warming. Figure 2b shows the
 254 corresponding precipitation sensitivity, which is defined as the change relative to the present
 255 climate, normalized by surface temperature increase. The sensitivity near the first peak is
 256 close to zero. However, the precipitation sensitivity related to the second precipitation
 257 maximum has shown large sensitivity and can reach up to 34.65% K^{-1} in the mid-term future
 258 and up to 43.41% K^{-1} in the long-term future. The response to warming is discussed in depth

259 in the next section. The remaining discussion of this section identify and explain essential
 260 mechanisms involved in shaping the distribution pattern of precipitation in our simulations.



261

262 Fig. 3. The zonal and temporal mean of (a) vertical velocity (w), (b) water vapor mixing ratio
 263 tendency due to microphysics (color shading), the sum of cloud ice (q_i) and cloud water (q_c)
 264 mixing ratio (contours, unit in g/kg), (c) mixing ratio of precipitation hydrometeors which
 265 include rain, graupel and snow (color shading) and graupel mixing ratio alone (contours, unit in
 266 g/kg).

267 Here, the mean states are firstly investigated. Figure 3a shows the zonal and temporal mean
 268 of vertical velocity. Two areas exhibit strong updrafts: 1) over the upwind slope of the
 269 mountain and 2) over the lee slope of the mountain centered at $y = 8$ km, $z = 5$ km. In
 270 downstream region away from the mountain, the averaged vertical velocity oscillates between
 271 positive and negative velocities, suggesting the presence of mountain-induced gravity waves.
 272 Those stationary updrafts and downdrafts weaken with distance away from the mountain and
 273 are confined below the tropopause, which indicates these lee waves are trapped, or at least
 274 partially trapped. The zonal and temporal mean of water vapor tendency due to microphysics
 275 (\dot{q}) is shown in Fig. 3b. The negative \dot{q} value indicates condensation and deposition whereas
 276 the positive \dot{q} values indicate evaporation and sublimation. Hereafter, the sum of the

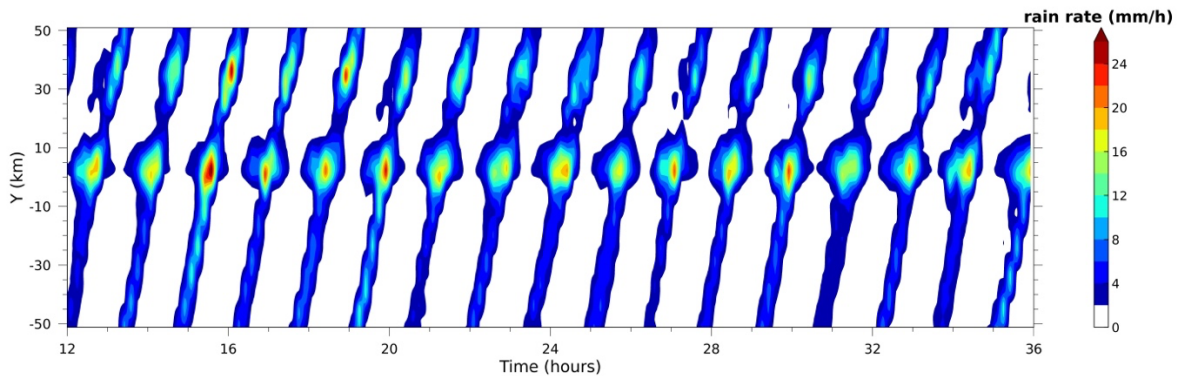
277 condensation rates and the deposition rates is referred as condensation-and-deposition rates.
278 The areas that exhibit strong updrafts also show strong condensation-and-deposition rates.
279 The two strong condensation-and-deposition centers caused by the strong stationary updrafts
280 correspond to the two cloud centers indicated by the sum of cloud water mixing ratio (q_c) and
281 ice mixing ratio (q_i). It is noteworthy that the two cloud centers exist throughout our
282 simulation and are closely related to two precipitation maxima.

283 As shown in Fig. 3c, the two precipitation peaks also correspond to the two regions with high
284 mixing ratios of precipitation hydrometeors (q_p). The q_p is the sum of mixing ratio of
285 rainwater (q_r), graupel (q_g) and snow (q_s). The high q_p region over the lee slope of the
286 mountain extends from the surface to the lower troposphere, suggesting ice phase process is
287 not involved much in the formation of the first precipitation peak. In contrast, the high q_p area
288 located in the downstream of the mountain extends from the surface up to upper troposphere.
289 A significant amount of graupel is found above the downstream precipitation region,
290 indicating the involvement of the ice and mixed phase processes in the formation of the
291 second precipitation peak. In the following subsection, we will show that the formation of the
292 two precipitation maxima is related to the interaction between the traveling mesoscale
293 disturbances and mountain wave-forced ascents, though the roles of them are different for the
294 two precipitation maxima.

295

296 *c. Traveling Mesoscale Disturbances*

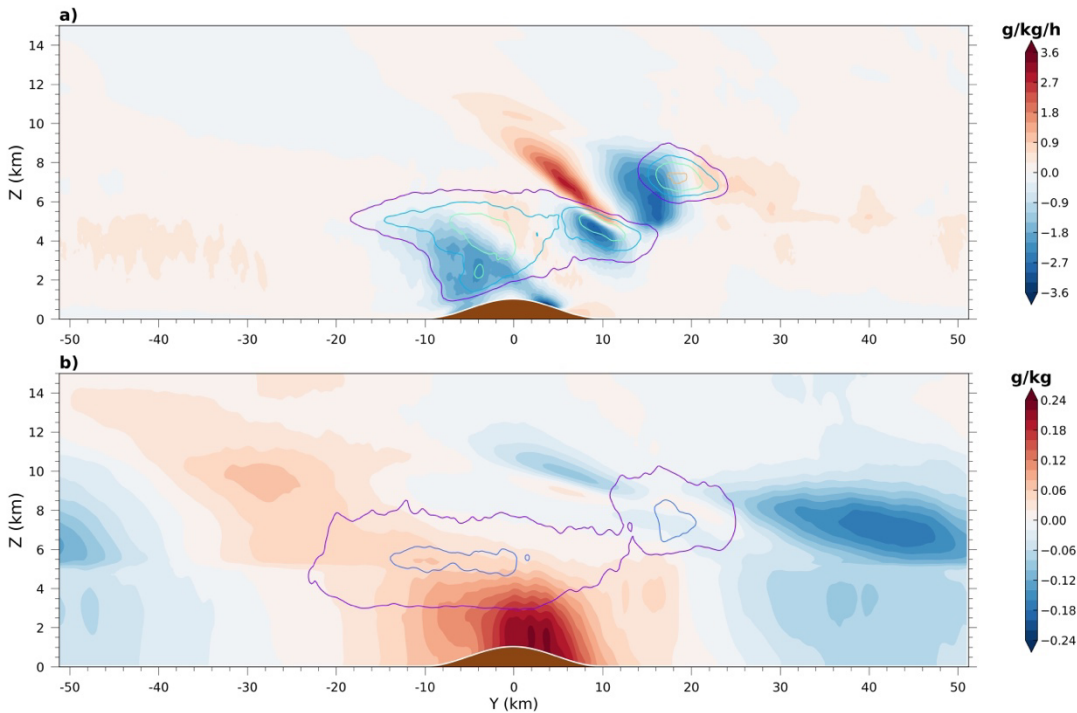
297 The Hovmöller diagram of the zonally averaged surface precipitation shows a precipitation
298 pattern suggesting northward traveling mesoscale disturbances (Fig. 4). The mesoscale
299 disturbances travel northward with a period of about 2 hours. In each cycle, the zonal mean
300 precipitation features the two precipitation maxima and a rain shadow region sandwiched by
301 the two-precipitation maxima. Notably, little-precipitation windows can be identified for
302 every location. The little-precipitation windows suggest that precipitation maxima are not
303 purely the result of the mean flow advection of hydrometeors produced in the two cloud
304 formation centers in Fig. 3b. Without the superposition of the traveling mesoscale
305 disturbances on the mean flow, little surface precipitation is generated, probably because of
306 insufficient microphysical conversion time (Zängl 2008) or evaporation when the
307 precipitation hydrometeors fall out of cloud at a high level (Kirshbaum and Smith 2008).



308

309 Fig. 4. The Hovmöller diagram of the zonally averaged surface precipitation in the present
310 climate simulation.

311 To further illustrate the relations between the two condensation centers and the two
312 precipitation maxima, regression analysis relating surface precipitation to hydrometeors (q_p ,
313 q_g , q_i+q_c) and \dot{q} has been conducted. Following Adames and Wallace (2014), the regression
314 map for each variable is derived from the equation, $\mathbf{D} = \mathbf{S} \mathbf{P}^T$, where \mathbf{D} is the two-
315 dimensional regression pattern for a two-dimensional matrix \mathbf{S} that represents a variable
316 field, and \mathbf{P} is a standardized time series of the variable being regressed upon.



317

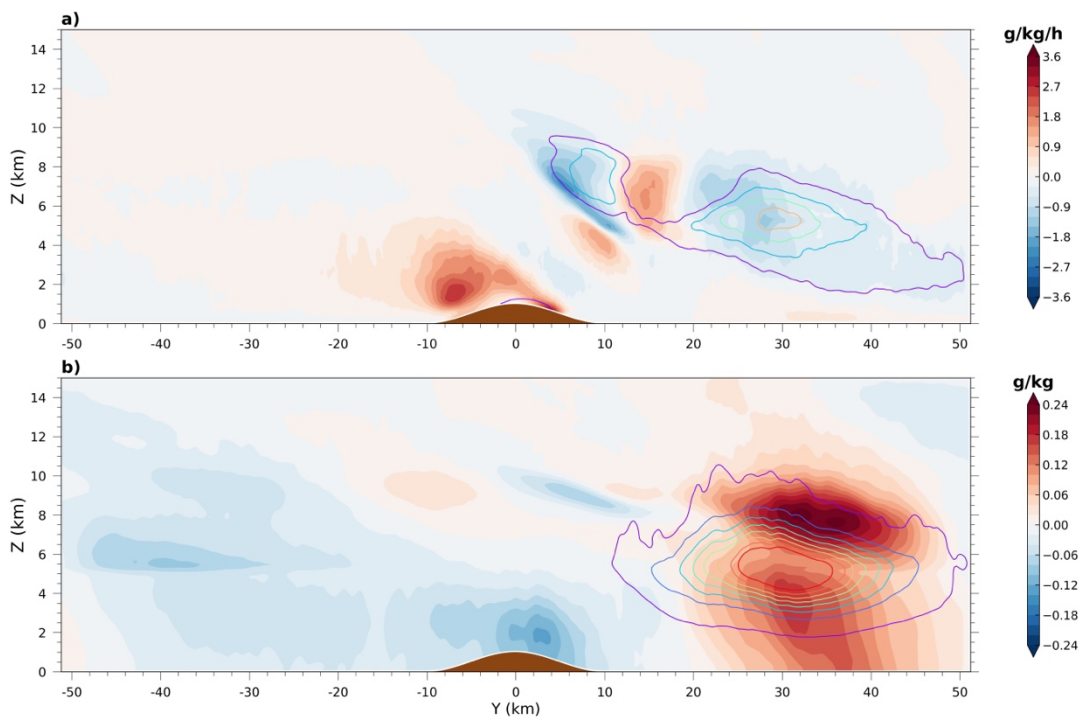
318 Fig. 5. Regression maps of water vapor tendency (\dot{q} ; color shading in (a)), mixing ratios of
319 ice and cloud water ($q_i + q_c$; contours in (a)), mixing ratios of precipitation hydrometeors (q_p ;
320 color shading in (b)) and mixing ratios of graupel (q_g ; contours in (b)) onto the time series of
321 mean precipitation over the mountain between $y = -14$ and $y = 10$ km in the present climate
322 simulation for. Contour interval in (a) is 0.04 g/kg and the purple contours indicate 0.04 g/kg.
323 Contour interval in (b) is 0.01g/kg and the purple contour indicates 0.001 g/kg.

324 The precipitation maximum over the mountain is related to the interaction between the cloud
325 above the windward slope of the mountain and the traveling mesoscale disturbances. The
326 regressed \dot{q} and $q_c + q_i$ in Fig. 5a show that low-level cloud formation is enhanced when there
327 is positive precipitation anomaly over the mountain. Noting that the regressed pattern
328 represents anomalies to be added to the stationary pattern in Fig. 3 when there is positive
329 precipitation anomaly on the mountain surface. Figure 5a suggests that when the mesoscale
330 disturbance reaches the mountain it probably triggers or enhances orographic convection
331 substantially and therefore enhance surface precipitation.

332 Meanwhile, the regression of precipitation hydrometeors (Fig. 5b) shows a second center of
333 positive anomaly at about 9 km above the surface and 30 km upstream of the mountain. The
334 upper level q_p anomaly extends downward until reaching the freezing level, but it also
335 extends downwind and connects with the low-level cloud and precipitation. Therefore, the
336 formation of effective precipitation over the mountain is likely also affected by the seeder-
337 feeder mechanism (Bergeron 1960). The upper-level regression anomaly in Fig. 5b suggests
338 stratiform precipitation in the upper and middle troposphere related to deep convective
339 system falls from above and enhances accretion in the low-level orographic cloud above then
340 windward slope. This regression pattern feature is also consistent with Fig. 4, which shows
341 that the precipitation over the mountain becomes notable before the main travelling
342 precipitation system reaches the mountain. The reason for which no deep convection signal
343 exists upstream of the mountain (from $y = -30$ km to $y = -20$ km) in the regression pattern is
344 probably because the regression has zero time lag, which makes the regressed pattern more
345 representative for features when precipitation over the mountain is maximized.

346 Figure 6 shows the regressed fields related to the precipitation in the downstream region,
347 which suggests the interaction between cloud induced by the mid-tropospheric orographic
348 ascent above the lee slope of the mountain (Fig. 3a) and the traveling convective system. The
349 negative anomaly of regressed \dot{q} and positive anomaly of regressed $q_c + q_i$ in Fig. 6a suggests
350 that deep convection exists when surface precipitation is enhanced in the downstream region.
351 The regressed q_p in Fig. 6b shows two maxima in the downstream region, one in the lower
352 troposphere and the other in the upper troposphere at about 8 km. The upper-level maximum
353 is related to the local deep convection. Interestingly, the lower-level maximum is somewhat
354 separated from the upper-level maximum, suggesting there is an additional mechanism that
355 enhances the lower-level precipitation hydrometeors mixing ratio. The presence of mid-

356 troposphere ascent and cloud formation above the lee slope of the mountain (Fig. 3b) can
 357 produce a significant amount of precipitation hydrometeors which drift downstream with the
 358 mean flow. As those hydrometeors fall into the lower and middle part of the convective
 359 system which develops in the downwind region, they enhance collision-and-coalescence or
 360 accretion like in the conventional seeder-feeder mechanism. We call this mechanism pseudo-
 361 seeder-feeder (PSF) mechanism because here convection and terrain forced ascents play roles
 362 differing from what they have in the conventional seed-feeder mechanism. The PSF
 363 mechanism is likely more important to local precipitation enhancement in the downwind
 364 region than over the mountain because the regression of graupel mixing ratio onto the second
 365 precipitation maximum in the downstream region (Fig. 6b) exhibits a substantially stronger
 366 signal than the same regression onto the first precipitation maximum over the mountain top
 367 (Fig. 5).



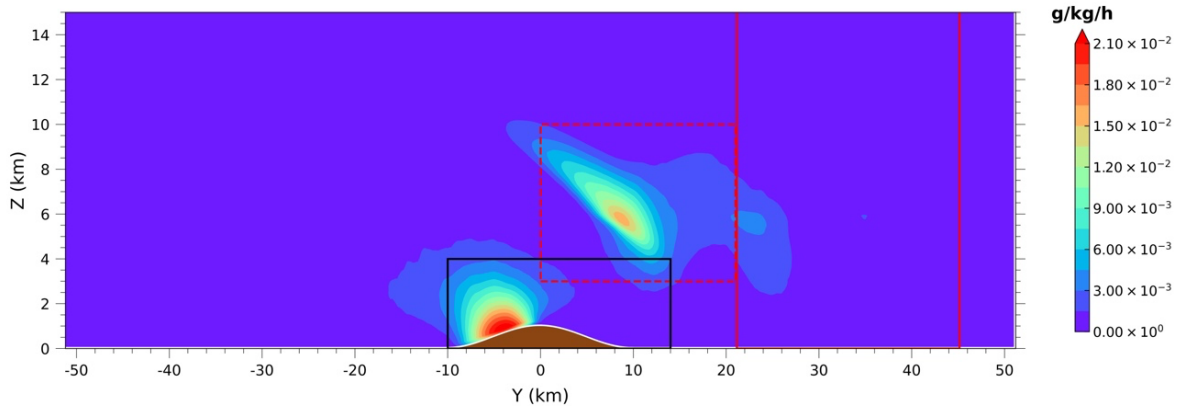
368
 369 Fig. 6. Same with Fig. 5, except that the variables are regressed onto the time-series of the
 370 mean precipitation in the downstream region between $y = 21$ and $y = 45$ km.

371

372 4. Precipitation Responses to Warming

373 As discussed in Section 3a, under warming, the precipitation over the downstream region and
 374 the mountain has strikingly different responses to warming. In this section, these two regions

375 are investigated separately to understand their responses to warming. Below, we calculate
 376 how the condensation-and-deposition rates change in the cloud formation region and how
 377 precipitation efficiency responds to warming. The impact of mountain waves is also
 378 discussed.



379

380 Fig. 7. The zonal and temporal mean of the sum of condensation and deposition rate in the
 381 simulation of present climate. The black box over the mountain is for the analysis of
 382 precipitation maximum over the mountain, and the region bounded by red lines between $y =$
 383 21 km and $y = 45$ km is for the analysis of precipitation over the downstream region. The red
 384 box between $y = 0$ km and $y = 21$ km wraps the condensation-and-deposition center in the lee
 385 of mountain.

386 *a. Over-Mountain Precipitation*

387 For the over-mountain precipitation region, the downstream transport of hydrometeors in a
 388 strong wind environment cannot be ignored because we are considering relatively small
 389 regions. We use the black box shown in Fig. 7 for a budget analysis. The box is bounded
 390 between $y = -10$ km and $y = 14$ km to include the first precipitation maximum and capped
 391 vertically at 4 km to avoid the inclusion of the lee condensation-and-deposition center in mid-
 392 troposphere to which the first precipitation maximum is unrelated. The time averaged surface
 393 precipitation (P) at the bottom of this box satisfies

$$P = C_{net} + F_{in} - F_{out} + R \quad (2)$$

394 where C_{net} is the volume integrated rate of net condensation and deposition, F_{in} (F_{out}) is the
 395 flux of condensates, including both non-precipitation and precipitation particles, into
 396 (leaving) the box through upstream (downstream) boundaries. C_{net} , F_{in} , and F_{out} are
 397 normalized with the bottom surface area of the box. R denotes the residual term due to
 398 ignoring surface evaporation and storage of hydrometeors in the air. This residual term can be
 399 minimized when we take the time average of a relatively long period so that the storage of

400 hydrometeors in the air can be ignored. Surface evaporation is also ignored because of its
 401 little contribution. The residual term only accounts for around 5% of the surface precipitation
 402 (Supplementary Table S1), suggesting the approximate balance between P and $C_{net} + F_{in} -$
 403 F_{out} inside the box. Including the influx of hydrometeors from upwind direction into the box,
 404 the PE is redefined as

$$PE = \frac{P}{F_{in} + C} \quad (3)$$

405 where F_{in} is influx convergence into the box, C is the volume integrated rate of condensation
 406 and deposition inside the box. Both C and F_{in} are normalized with the bottom surface area of
 407 the box. For this over-mountain precipitation region, C is much larger than F_{in} . Denoting the
 408 surface temperature by T_s , the total precipitation sensitivity can be decomposed as

$$\begin{aligned} \frac{1}{P} \frac{\partial P}{\partial T_s} &= \frac{\partial \ln P}{\partial T_s} = \frac{\partial \ln(PE \cdot (C + F_{in}))}{\partial T_s} = \frac{\partial \ln(C + F_{in})}{\partial T_s} + \frac{\partial \ln(PE)}{\partial T_s} \\ &= \frac{\partial(C + F_{in})}{(C + F_{in}) \partial T_s} + \frac{\partial PE}{PE \partial T_s} \end{aligned} \quad (4)$$

409 The precipitation sensitivity over the mountain is the sum of the sensitivity of $C + F_{in}$ and that
 410 of PE. Table 1 is the average sensitivity obtained by comparing the simulations of present and
 411 mid-term future and that by comparing those of present and long-term future. As shown in
 412 Table 1, both terms have shown sensitivities less than 1% K⁻¹. Therefore, the weak
 413 precipitation response to warming is due to small sensitivities of PE, F_{in} , and C . The C in the
 414 black box has shown a slight decrease with warming. This negative sensitivity is at odds with
 415 the expected positive sensitivity in previous studies (e.g., Siler and Roe, 2014). To understand
 416 the negative condensation sensitivity to the warming, the change of C in the black box is
 417 further decomposed to thermodynamic and dynamic contributions based on the methodology
 418 in Shi and Durran (2015). The thermodynamic contribution is related to the change in the
 419 moist adiabatic lapse rate of saturation water vapor specific humidity (γ) due to temperature
 420 increase, and the dynamic contribution is related to the change in the vertical velocity (Muller
 421 and Takayabu, 2020; Shi and Durran, 2015). Our calculation found that the thermodynamic
 422 contribution is at around 2.11% K⁻¹, which is offset by the dynamic contribution at around
 423 -2.68% K⁻¹. The temperature of the upslope condensation center in our black box ranges
 424 from ~270 to ~300 K. Our calculation of thermal contribution to the warming is consistent
 425 with the γ sensitivity in that temperature range (shown in Fig. 12 of Shi and Durran (2014)).

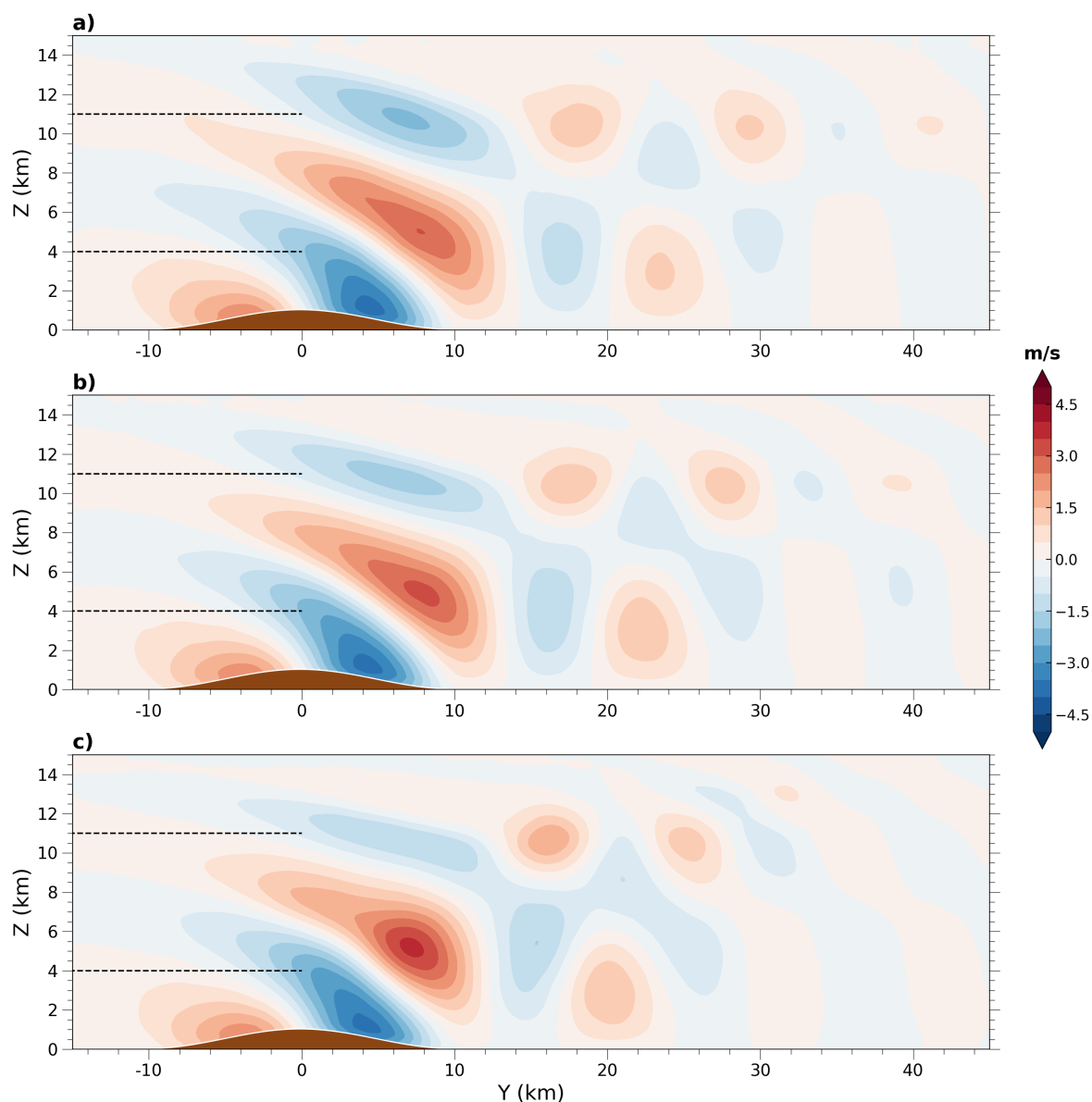
426

427 Table 1: Sensitivity with respect to surface warming over the mountain region (indicated by
428 the black solid box in Fig. 7): precipitation (P), the sum of condensation and deposition rates
429 (C), flux into the black solid box from the upstream boundary (F_{in}), precipitation efficiency
430 (PE). C_t is the thermodynamic contribution of C . C_d is the dynamic contribution of C .

Sensitivity (% K ⁻¹)	P	C	F_{in}	$C+F_{in}$	PE	C_t	C_d
Mid-term	0.69	-0.29	0.66	-0.14	0.84	2.16	-2.55
Long-term	-1.81	-1.32	1.00	-0.97	-0.86	2.07	-2.81
Mean	-0.56	-0.80	0.83	-0.56	-0.01	2.11	-2.68

431

432 The negative dynamic contribution is related to the weakening of vertical velocities over the
433 windward slope of the mountain under warming. The zonal and temporal mean of vertical
434 velocities are shown in Fig. 8. The mean vertical velocity maximum over the windward slope
435 of the mountain does not exhibit appreciable change but the depth of the ascending layer
436 shallows in response to warming. The weakening of vertical velocities is probably related to
437 the response of mountain wave to the increased stability (Shi and Durran 2015), which is
438 caused by the amplified warming in the upper troposphere. Additionally, negative dynamic
439 contribution is also found in the previous study of extreme convective precipitation in the
440 tropics (Muller et al., 2011).



441

442 Fig. 8. The zonal and temporal mean of vertical velocities of simulations of the climate of the
 443 present (a), mid-term (b), and long-term future (c). The black dash lines at 4 km and 11 km
 444 are for height references.

445

446 *b. Downstream Region Precipitation.*

447 In the downstream precipitation maximum region, we conduct the same budget analysis for
 448 precipitation efficiency and hydrometeor production. The budget box is defined starting from
 449 21 km to 45 km in the y direction, which is indicated by the red solid vertical lines in Fig. 7.
 450 The downstream precipitation statistics are partly shown in Supplementary Table S2.

451 The precipitation in the downstream has exhibited substantial change due to warming, and as
452 shown in Table 2, the mean precipitation sensitivity is at 18.16% K⁻¹. The local C has shown
453 little change and its mean sensitivity to the warming is at -0.29% K⁻¹. In contrast, the F_{in}
454 sensitivity is at 9.25% K⁻¹, suggesting the increased influx with warming. The F_{in} increase
455 can be explained by the increased condensation and deposition rate in the lee-slope mid-
456 troposphere condensation-and-deposition center C_2 (denoted by the red dashed box in Fig. 7).
457 The sensitivities of C_2 are consistent with the F_{in} (Table 2), indicating that the influx increase
458 is due to the amplification of C_2 . We further decompose the change of the C_2 into
459 thermodynamic and dynamic contributions. The dynamic contribution is slightly positive and
460 at 1.04 % K⁻¹, while the thermodynamic contribution is at 7.20 % K⁻¹, revealing that the
461 increase of influx is primarily from thermodynamic contribution. The thermodynamic
462 sensitivity of C_2 is larger than that of the low-level windward slope condensation center
463 because 1) the sensitivity of γ to temperature is higher at colder temperatures (Fig. 12 of Shi
464 and Durran (2014)) and 2) mid-troposphere exhibits stronger temperature increase than the
465 surface.

466 Table 2: Sensitivity with respect to surface warming in the downstream region (indicated by
467 the red solid box in Fig. 7): precipitation (P), condensation (C), flux into the red solid box
468 from the upstream boundary (F_{in}), precipitation efficiency (PE). The C_2 is condensation rate
469 of the red dashed box region shown in Fig. 7. C_{2t} is the thermodynamic contribution of C_2 .
470 C_{2d} is the dynamic contribution of C_2 .

Sensitivity (% K ⁻¹)	P	C	F_{in}	$C+F_{in}$	PE	C_2	C_{2t}	C_{2d}
Mid-term	19.37	-0.83	12.02	6.32	12.14	11.52	7.99	1.29
Long-term	16.96	-1.42	6.49	2.46	13.34	6.80	6.41	0.79
Mean	18.16	-0.29	9.25	4.39	12.74	9.16	7.20	1.04

471
472 Following Eq. (4), the precipitation sensitivity in the downstream region can also be
473 decomposed into the sensitivity related to PE change and source of hydrometeors ($C + F_{in}$).
474 The change in precipitation efficiency is dominant at 12.74% K⁻¹, while the change of the
475 sum of local condensation and influx plays a secondary role at 4.39% K⁻¹(Table 2). The high
476 PE sensitivity suggests enhancement of the pseudo seeder-feeder effects. This enhancement is

477 probably due to the increases of F_{in} into the downstream region that can be further attributed
478 to the amplified lee cloud formation center C_2 .

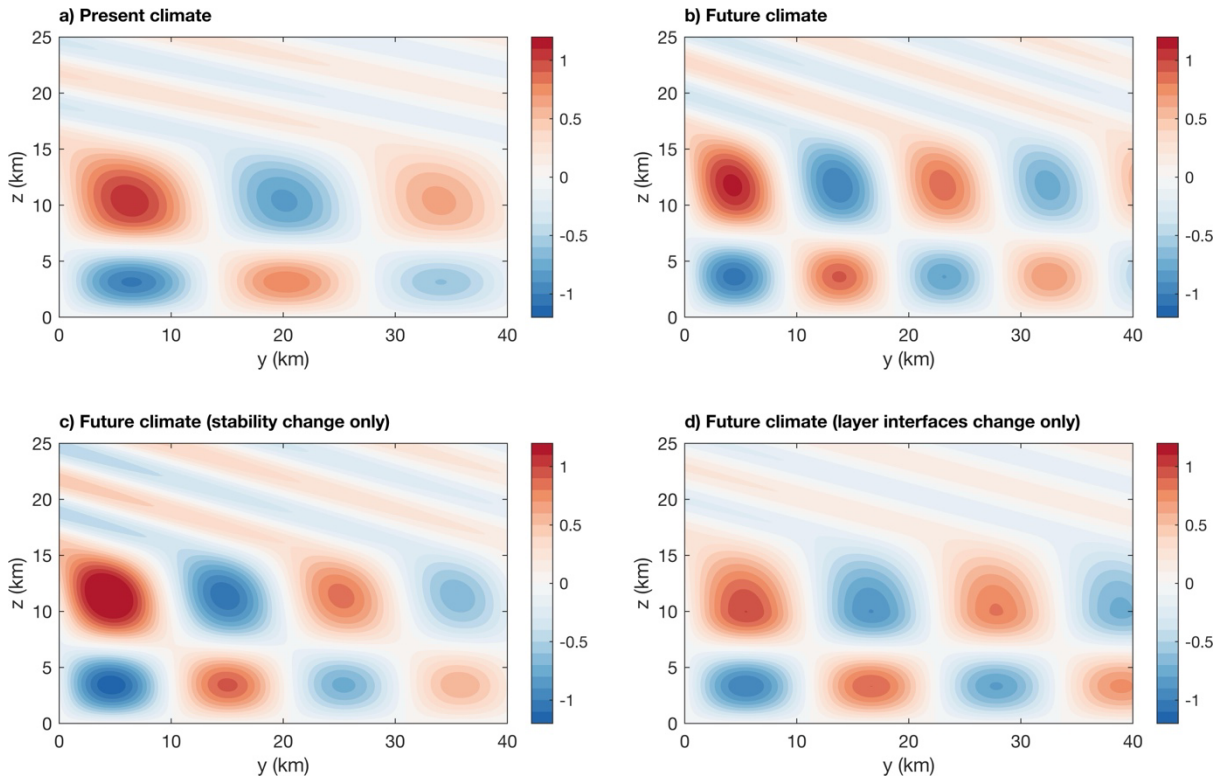
479 The high precipitation peak sensitivity in the downstream region is also partially due to the
480 upwind shift of the second precipitation maximum, which exhibits ~ 10 km between the
481 present and long-term future simulations. This upwind shift of downstream region
482 precipitation peak is related to the upwind shift of mean state mountain waves and the lifting
483 of freezing level in the warmed climates. The mean state wave patterns of vertical velocities
484 are shown in Fig. 8. The updraft centered at $y \approx 24$ km in the simulation of present climate
485 moves upwind to $y \approx 20$ km in the simulation in of long-term future climate. With the
486 upwind shift of mean state waves, the region which is prone to the development of new
487 convection in the downstream region moves upwind. The hydrometeors drifting from the lee
488 mid-troposphere center will travel at a shorter distance and experience less evaporation or
489 sublimation before seeding the low-level convection in the downstream region. In addition, as
490 the freezing level shifts upward, the fraction of liquid-phase hydrometeors increases in the lee
491 slope mid-troposphere cloud center. As a result, the seeder hydrometeors fall at relatively
492 larger terminal velocity and tend to interact with the low-level feeder clouds earlier at a
493 shorter travel distance in the horizontal direction.

494 **5. Upwind Shift of Trapped Lee Waves**

495 The upwind shift of downstream precipitation maximum is, at least partially, related to the
496 upwind shift of trapped lee waves, which is investigated in this section with the numerical
497 methods of Durran et al. (2015), which search for linear modes that represent trapped waves
498 in the lee of a mountain.

499 We used a 3-layer setup for the linear model, with layer interfaces at 9 km and 16 km for the
500 present climate, and 10 km and 17 km for the long-term future climate. The moist squared
501 Brunt–Väisälä frequency N^2 for the present climate setup is 1.2, 0.5, and $5 \times 10^{-4} \text{ s}^{-2}$ for the
502 three layers from bottom to top. For the long-term future scenario, the mid-layer N^2 increases
503 from $0.5 \times 10^{-4} \text{ s}^{-2}$ to $0.8 \times 10^{-4} \text{ s}^{-2}$. The N^2 in other layers is the same as the present climate
504 setup. The horizontal wind is assumed as 20 m/s at all layers. This assumption of the wind
505 profile is the main caveat that we cannot avoid because in three-dimensional CM1
506 simulations we have both u and v velocity components, but we can only have one horizontal
507 direction in the two-dimensional model. These parameters are idealization based on the
508 simulation data. The method of Durran et al. (2015) yields two trapped modes for each setup.

509 However, one of them has only one vertical velocity extremum in the troposphere and is not
 510 consistent with the mean velocity pattern in Fig. 8.



511

512 Fig.9. Contours of normalized vertical velocities in a vertical cross section obtained using
 513 the numerical methods developed by Durran et al., (2015). (a) Calculations based on the
 514 stability parameters and the layer interfaces of the present climate. (b) Calculations based on
 515 the stability parameters and the layer interfaces of the long-term future climate. (c)
 516 Calculations based on the stability parameters of the long-term future climate but the layer
 517 interfaces of present climate. (d) Calculations based on the stability parameters of the present
 518 climate but the layer interfaces of the long-term future climate.

519

520 Figure 9 shows the relevant solution of the trapped mode, which indeed exhibits upwind shift
 521 under global warming. The upwind shift of trapped lee waves is due to the decrease in the
 522 horizontal wavelength of trapped lee waves. The resonant wavelength decreases from the
 523 27.6 km in the present climate setup to the 18.7 km in the long-term future climate set-up.
 524 The effects of increasing upper troposphere (the middle layer in the 3-layer setup) static
 525 stability and lifted layer interfaces are separately evaluated in Fig. 9c and 9d, while Fig. 9b is
 526 the composite effect. Both factors contribute to the decrease of the resonant wavelength. If
 527 we only change the stability N^2 while keeping the layer interface heights unchanged, the
 528 resonant wavelength decreases to 20.4 km. If the layer interfaces are changed while the
 529 stability is kept constant, the resonant wavelength decreases to 22.1 km. Therefore, the

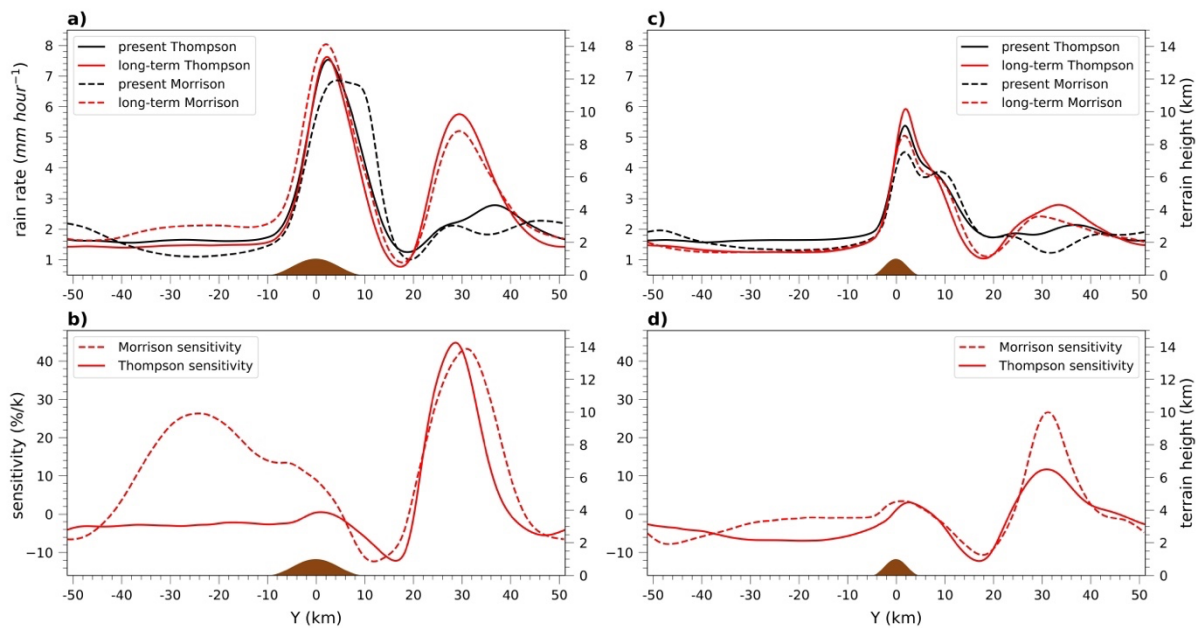
530 stability enhancement is probably more important to induce the upwind shift of trapped lee
531 waves, though the role of lifted layer interfaces is also nonnegligible.

532 **6. Robustness of Results**

533 The robustness of our results is tested using the Morrison microphysics scheme and a
534 narrower mountain (NM). Consistently, the highest precipitation sensitivity happens in the
535 downstream region (Fig. 10).

536 Figure 10a shows the zonal and temporal rainfall distribution in the simulations using the
537 Morrison microphysical scheme. Different from the Thompson scheme, the second
538 precipitation maximum in the downstream of the mountain in Morrison is weak and virtually
539 non-existent. The discrepancy in the occurrence of precipitation maximum in the downstream
540 region in the simulation of present climate is probably related to the different liquid to solid
541 ratios of the seeder particles in these two microphysical schemes. The transition of seeding
542 precipitation particles from the solid phase to the liquid phase happens in an earlier stage in
543 the Morrison scheme (Supplementary Fig. S2). As a result, a higher liquid ratio in the seeding
544 precipitation particles is expected in the Morrison scheme. Given the ice particles involved
545 processes are more efficient in producing rainwater (Kirshbaum and Smith 2008), the PSF in
546 the Morrison scheme is expected to be weaker and thus may fail to create the downstream
547 precipitation peak.

548 Experiments using a narrower mountain with a half-width of 5 km (NM) are also tested with
549 different microphysical schemes. Previous experiments using the 10 km mountain half-width
550 are referred as the wide mountain (WM). The two cloud formation centers induced by the
551 NM are much smaller (Supplementary Fig. S2). With smaller cloud formation centers, both
552 the traditional seeder-feeder effects and PSF are weakened and therefore weaker precipitation
553 is resulted in the NM simulations (shown in Fig. 10a and Fig. 10c). Interestingly, in the
554 present climate of NM, both microphysics schemes do not produce the downstream
555 precipitation maximum. This is probably because the weaker lee cloud formation center
556 supplies fewer drifting hydrometeors which serve as seeder particles in PSF. Although the
557 solid particle fraction in present climate is higher than that in warmed climates. This
558 advantageous condition for enhanced PSF is outweighed by the weaker lee cloud formation
559 center in the present climate.



560

561 Fig. 10. The temporal and zonal mean precipitation in the simulation of present and long-
 562 term future climate, and corresponding precipitation sensitivity using different half widths of
 563 the mountain range and microphysical schemes. The half width of 10 km using the
 564 Thompson and Morrison scheme (a), (b). The half width of 5 km using Thompson scheme
 565 and Morrison scheme in (c) (d).

566

567 7. Conclusions

568 The global warming response of orographic precipitation induced by the interaction between
 569 a typhoon's outer circulation environment and a mountain is estimated with pseudo-global
 570 warming experiments using LES. In our control simulation for the present climate, the cross-
 571 mountain direction precipitation distribution exhibits two maxima with first maximum
 572 located on the lee slope of the mountain and the second weaker maximum in the region
 573 downstream of the mountain. The first precipitation maximum is related to the conventional
 574 seeder-feeder effect and enhanced convection by the mountain. The second maximum is
 575 related to a pseudo seeder-feeder effect in which the seeder cloud is the mountain wave
 576 induced mid-troposphere cloud above the lee slope and feeder cloud is the middle and lower
 577 part of traveling precipitation system in the downstream region.

578 In response to the warming, the first rainfall maximum exhibits almost no change because
 579 both condensation rate and precipitation efficiency have negligible changes. This weak
 580 sensitivity of condensation rate is because the positive thermodynamic contribution is
 581 canceled by the negative dynamic contribution. In contrast, the second rainfall maximum

582 shifts upwind and intensifies significantly. The precipitation sensitivity in the downstream
583 region (21 km to 45 km away from mountain) is at 18.16% K⁻¹ on average and has a
584 maximum sensitivity up to 43.41% K⁻¹. In the downstream region, the accelerated rainfall
585 intensification is attributed to the substantial amplification of the condensation-and-
586 deposition center in the mid-troposphere above the lee slope, where the temperature is lower
587 than the low-level condensation center and the thermodynamic sensitivity is relatively high.
588 This enhancement increases the downstream precipitation by increasing the influx of
589 hydrometeors and thereby enhancing the pseudo seeder-feeder effect.

590 The high peak sensitivity in downstream region precipitation is also partially due to the
591 upwind shift of the precipitation maximum, which is caused by the upwind shift of the
592 trapped lee waves and the lifting of the freezing level. The upwind shift of trapped lee waves
593 is further corroborated by a three-layer linear mountain wave model, which shows a decrease
594 in the resonant wavelength of the trapped lee wave due to the lifting of the layer interfaces
595 and the increase in upper tropospheric stability.

596 The robustness of our results is tested with a narrower mountain and a different microphysics
597 scheme. Consistently, all simulations in warmed climate show relatively larger precipitation
598 sensitivity in the downstream region. Lee side regeneration of convection has been
599 investigated in previous studies (Houze 2012). However, the contribution from mountain
600 wave induced lee-slope mid-troposphere cloud to the downstream region precipitation is
601 neglected in previous studies, probably because precipitation particles may evaporate
602 completely before reaching low-level cloud and thereby the pseudo seeder-feeder mechanism
603 is not activated.

604 Our estimation of future orographic precipitation in the typhoon outer region environment
605 shows that the greatest precipitation sensitivity happens in the downstream area, while the
606 precipitation maximum over the mountain stays almost unchanged with warming. Although
607 these are idealized experiments, our findings suggest plausible mechanisms by which the
608 precipitation maximum in the downstream region of mountain barriers may emerge and
609 intensify substantially under warming. Those mechanisms warrant further investigations
610 focusing on the downstream region of mountains in the context of flooding risk management
611 under climate change.

612

613

614 *Acknowledgments.*

615 This research was funded by the Research Grants Council of Hong Kong SAR, China
616 (Project Nos. AoE/E-603/18 and HKUST 26305720).

617

618 *Data Availability Statement.*

619 The CM1 code and namelist files can be found at
620 <https://github.com/JiananChenUST/Chen-and-Shi-2023-.git>. The initial input profiles are also
621 included.

622

623 REFERENCES

624 Adames, Á. F., and J. M. Wallace, 2014: Three-Dimensional Structure and Evolution of the
625 MJO and Its Relation to the Mean Flow. *Journal of the Atmospheric Sciences*, **71**,
626 2007–2026, <https://doi.org/10.1175/JAS-D-13-0254.1>.

627 Beniston, M., 2005: Mountain Climates and Climatic Change: An Overview of Processes
628 Focusing on the European Alps. *Pure appl. geophys.*, **162**, 1587–1606,
629 <https://doi.org/10.1007/s00024-005-2684-9>.

630 Bergeron, T., 1960: Problems and Methods of Rainfall Investigation Address of the Honorary
631 Chairman of the Conference. *Geophysical Monograph Series*, H. Weickmann, Ed.,
632 American Geophysical Union, 5–30.

633 Bryan, G. H., and J. M. Fritsch, 2002: A Benchmark Simulation for Moist Nonhydrostatic
634 Numerical Models. *Mon. Wea. Rev.*, **130**, 2917–2928, [https://doi.org/10.1175/1520-0493\(2002\)130<2917:ABSFMN>2.0.CO;2](https://doi.org/10.1175/1520-0493(2002)130<2917:ABSFMN>2.0.CO;2).

636 ———, R. P. Worsnop, J. K. Lundquist, and J. A. Zhang, 2017: A Simple Method for
637 Simulating Wind Profiles in the Boundary Layer of Tropical Cyclones. *Boundary-
638 Layer Meteorol*, **162**, 475–502, <https://doi.org/10.1007/s10546-016-0207-0>.

639 Chen, X., G. H. Bryan, J. A. Zhang, J. J. Cione, and F. D. Marks, 2021: A Framework for
640 Simulating the Tropical-Cyclone Boundary Layer Using Large-Eddy Simulation and
641 Its Use in Evaluating PBL Parameterizations. *Journal of the Atmospheric Sciences*,
642 <https://doi.org/10.1175/JAS-D-20-0227.1>.

643 Chow, F., C. Schär, N. Ban, K. Lundquist, L. Schlemmer, and X. Shi, 2019: Crossing
644 Multiple Gray Zones in the Transition from Mesoscale to Microscale Simulation over
645 Complex Terrain. *Atmosphere*, **10**, 274, <https://doi.org/10.3390/atmos10050274>.

646 Deardorff, J. W., 1980: Stratocumulus-capped mixed layers derived from a three-dimensional
647 model. *Boundary-Layer Meteorol*, **18**, 495–527, <https://doi.org/10.1007/BF00119502>.

- 648 Durrán, D. R., M. O. G. Hills, and P. N. Blossey, 2015: The Dissipation of Trapped Lee
649 Waves. Part I: Leakage of Inviscid Waves into the Stratosphere. *Journal of the*
650 *Atmospheric Sciences*, **72**, 1569–1584, <https://doi.org/10.1175/JAS-D-14-0238.1>.
- 651 Eidhammer, T., V. Grubišić, R. Rasmussen, and K. Ikdea, 2018: Winter Precipitation
652 Efficiency of Mountain Ranges in the Colorado Rockies Under Climate Change. *J.*
653 *Geophys. Res. Atmos.*, **123**, 2573–2590, <https://doi.org/10.1002/2017JD027995>.
- 654 Guichard, F., and F. Couvreux, 2017: A short review of numerical cloud-resolving models.
655 *Tellus A: Dynamic Meteorology and Oceanography*, **69**, 1373578,
656 <https://doi.org/10.1080/16000870.2017.1373578>.
- 657 Hong Kong Observatory, 2012: Report on Severe Typhoon Vicente. Accessed 10 December
658 2022, <https://www.hko.gov.hk/en/informtc/vicente/vicente.htm>
- 659 Houze, R. A., 2012: Orographic effects on precipitating clouds. *Rev. Geophys.*, **50**, RG1001,
660 <https://doi.org/10.1029/2011RG000365>.
- 661 Iacono, M. J., J. S. Delamere, E. J. Mlawer, M. W. Shephard, S. A. Clough, and W. D.
662 Collins, 2008: Radiative forcing by long-lived greenhouse gases: Calculations with
663 the AER radiative transfer models. *J. Geophys. Res.*, **113**, D13103,
664 <https://doi.org/10.1029/2008JD009944>.
- 665 Ji, F., and Coauthors, 2020: Projected changes in vertical temperature profiles for Australasia.
666 *Clim Dyn*, **55**, 2453–2468, <https://doi.org/10.1007/s00382-020-05392-2>.
- 667 Jing, X., B. Geerts, Y. Wang, and C. Liu, 2019: Ambient Factors Controlling the Wintertime
668 Precipitation Distribution across Mountain Ranges in the Interior Western United
669 States. Part II: Changes in Orographic Precipitation Distribution in a Pseudo-Global
670 Warming Simulation. *Journal of Applied Meteorology and Climatology*, **58**, 695–715,
671 <https://doi.org/10.1175/JAMC-D-18-0173.1>.
- 672 Kirshbaum, D., B. Adler, N. Kalthoff, C. Barthlott, and S. Serafin, 2018: Moist Orographic
673 Convection: Physical Mechanisms and Links to Surface-Exchange Processes.
674 *Atmosphere*, **9**, 80, <https://doi.org/10.3390/atmos9030080>.
- 675 Kirshbaum, D. J., and R. B. Smith, 2008: Temperature and moist-stability effects on
676 midlatitude orographic precipitation. *Q.J.R. Meteorol. Soc.*, **134**, 1183–1199,
677 <https://doi.org/10.1002/qj.274>.
- 678 Lin, Y.-L., R. L. Deal, and M. S. Kulie, 1998: Mechanisms of Cell Regeneration,
679 Development, and Propagation within a Two-Dimensional Multicell Storm.
680 *JOURNAL OF THE ATMOSPHERIC SCIENCES*, **55**, 20.
- 681 Mallen, K. J., M. T. Montgomery, and B. Wang, 2005: Reexamining the Near-Core Radial
682 Structure of the Tropical Cyclone Primary Circulation: Implications for Vortex
683 Resiliency. *Journal of the Atmospheric Sciences*, **62**, 408–425,
684 <https://doi.org/10.1175/JAS-3377.1>.
- 685 Morrison, H., G. Thompson, and V. Tatarskii, 2009: Impact of Cloud Microphysics on the
686 Development of Trailing Stratiform Precipitation in a Simulated Squall Line:

- 687 Comparison of One- and Two-Moment Schemes. *Monthly Weather Review*, **137**,
688 991–1007, <https://doi.org/10.1175/2008MWR2556.1>.
- 689 Muller, C., 2013: Impact of Convective Organization on the Response of Tropical
690 Precipitation Extremes to Warming. *Journal of Climate*, **26**, 5028–5043,
691 <https://doi.org/10.1175/JCLI-D-12-00655.1>.
- 692 ———, and Y. Takayabu, 2020: Response of precipitation extremes to warming: what have we
693 learned from theory and idealized cloud-resolving simulations, and what remains to
694 be learned? *Environ. Res. Lett.*, **15**, 035001, [https://doi.org/10.1088/1748-](https://doi.org/10.1088/1748-9326/ab7130)
695 [9326/ab7130](https://doi.org/10.1088/1748-9326/ab7130).
- 696 Muller, C. J., P. A. O’Gorman, and L. E. Back, 2011: Intensification of Precipitation
697 Extremes with Warming in a Cloud-Resolving Model. *Journal of Climate*, **24**, 2784–
698 2800, <https://doi.org/10.1175/2011JCLI3876.1>.
- 699 O’Gorman, P. A., 2015: Precipitation Extremes Under Climate Change. *Curr Clim Change*
700 *Rep*, **1**, 49–59, <https://doi.org/10.1007/s40641-015-0009-3>.
- 701 Pavelsky, T. M., S. Sobolowski, S. B. Kapnick, and J. B. Barnes, 2012: Changes in
702 orographic precipitation patterns caused by a shift from snow to rain: OROGRAPHIC
703 PRECIPITATION PATTERNS. *Geophys. Res. Lett.*, **39**,
704 <https://doi.org/10.1029/2012GL052741>.
- 705 Rasmussen, R., and Coauthors, 2011: High-Resolution Coupled Climate Runoff Simulations
706 of Seasonal Snowfall over Colorado: A Process Study of Current and Warmer
707 Climate. *Journal of Climate*, **24**, 3015–3048,
708 <https://doi.org/10.1175/2010JCLI3985.1>.
- 709 Schär, C., and C. Frei, 2005: Orographic Precipitation and Climate Change. *Global Change*
710 *and Mountain Regions*, U.M. Huber, H.K.M. Bugmann, and M.A. Reasoner, Eds.,
711 Vol. 23 of *Advances in Global Change Research*, Springer Netherlands, 255–266.
- 712 ———, ———, D. Lüthi, and H. C. Davies, 1996: Surrogate climate-change scenarios for
713 regional climate models. *Geophys. Res. Lett.*, **23**, 669–672,
714 <https://doi.org/10.1029/96GL00265>.
- 715 Shi, X., and D. R. Durran, 2014: The Response of Orographic Precipitation over Idealized
716 Midlatitude Mountains Due to Global Increases in CO₂. *Journal of Climate*, **27**,
717 3938–3956, <https://doi.org/10.1175/JCLI-D-13-00460.1>.
- 718 ———, and ———, 2015: Estimating the Response of Extreme Precipitation over Midlatitude
719 Mountains to Global Warming. *Journal of Climate*, **28**, 4246–4262,
720 <https://doi.org/10.1175/JCLI-D-14-00750.1>.
- 721 ———, and Y. Wang, 2022: Impacts of Cumulus Convection and Turbulence
722 Parameterizations on the Convection-Permitting Simulation of Typhoon Precipitation.
723 *Monthly Weather Review*, <https://doi.org/10.1175/MWR-D-22-0057.1>.

- 724 Siler, N., and G. Roe, 2014: How will orographic precipitation respond to surface warming?
725 An idealized thermodynamic perspective. *Geophys. Res. Lett.*, **41**, 2606–2613,
726 <https://doi.org/10.1002/2013GL059095>.
- 727 Smith, R. B., P. Schafer, D. Kirshbaum, and E. Regina, 2009: Orographic Enhancement of
728 Precipitation inside Hurricane Dean. *Journal of Hydrometeorology*, **10**, 820–831,
729 <https://doi.org/10.1175/2008JHM1057.1>.
- 730 Thompson, G., P. R. Field, R. M. Rasmussen, and W. D. Hall, 2008: Explicit Forecasts of
731 Winter Precipitation Using an Improved Bulk Microphysics Scheme. Part II:
732 Implementation of a New Snow Parameterization. *Monthly Weather Review*, **136**,
733 5095–5115, <https://doi.org/10.1175/2008MWR2387.1>.
- 734 Trapp, R. J., M. J. Woods, S. G. Lasher-Trapp, and M. A. Grover, 2021: Alternative
735 Implementations of the “Pseudo-Global-Warming” Methodology for Event-Based
736 Simulations. *JGR Atmospheres*, **126**, <https://doi.org/10.1029/2021JD035017>.
- 737 Wang, Y., Y. Wang, and H. Fudeyasu, 2009: The Role of Typhoon Songda (2004) in
738 Producing Distantly Located Heavy Rainfall in Japan*. *Monthly Weather Review*,
739 **137**, 3699–3716, <https://doi.org/10.1175/2009MWR2933.1>.
- 740